Doppler-Free Spectroscopy of Hyperfine Zeeman Effects in Rubidium

Samuel Bader and Leo Zhou
MIT Department of Physics
(Dated: May 19, 2013)

The hyperfine Zeeman effect is observed via Doppler-free spectroscopy on the D2 line of rubidium. The effect is quantified by measurements of the gyromagnetic ratios of the electronic angular momentum in the $5^2S_{1/2}$ and $5^2P_{3/2}$ states, which are in agreement with previous accepted values.

I. INTRODUCTION

As demonstrated in [2], Doppler-free spectroscopy is a powerful technique which brings hyperfine atomic structure (at scales as small as tens of megahertz for the rubidium $5^2P_{3/2}$ level) within the reach of room temperature laser spectrosropy. Given easily acheivable magnetic fields, Zeeman effects in rubidium may reach the same magnitude; so, as proposed in [3], we will employ this technique upon the rubidium D2 line ($5^2S_{1/2}$ to $5^2P_{3/2}$) in order to measure the Zeeman effect in rubidium.

The combined Hamiltonian of hyperfine structure and Zeeman effects can be expressed as

$$H_{\mathrm{HF}} + H_{\mathrm{Z}} = hA\vec{I}\cdot\vec{J} + \frac{\mu_B}{\hbar}(g_J\vec{J} + g_I\vec{I})\cdot\vec{B}$$

where A is a hyperfine coupling constant, and g_J and g_I are respectively the electronic and nuclear gyromagnetic ratios.[1] The competition of hyperfine and Zeeman effects can be difficult to model when both are close enough in magnitude to void perturbation theory. To this end, we have numerically diagonalized the relevant terms of the Hamiltonian for the $5^2S_{1/2}$ and $5^2P_{3/2}$ states. The energies for ^{87}Rb are shown in Figure 1, and the reader is encouraged to refer back to the original proposal [3] for more details, since this report will focus on only the regions found here to be experimentally accessible.

The region of interest for this experiment will be fields in the range of 160-300G. Examination of the leftmost plot in Figure 1 shows that, for the $5^2S_{1/2}$ structure, with hyperfine splittings of several GHz, the Zeeman effect is a minor perturbation. The shifted energy levels can then be described to first order by an effective Zeeman term [6]

$$H = g_F m_F \mu_B B$$

where[2]

$$g_F = g_J \frac{F(F+1) - I(I+1) + J(J+1)}{2F(F+1)}$$

Note that this is the g_J *of the* $5^2S_{1/2}$ *state*. Next, examination of the rightmost plot in Figure 1 reveals that, in this same region of magnetic field, the Zeeman term actually dominates the $5^2P_{3/2}$ structure, and the shifted energies[3] can be described by [6]

$$H = g_J m_J \mu_B B$$

Where this is the g_J *of the* $5^2P_{3/2}$ *state*. So, as the magnetic field increases, the peaks corresponding to a transition from a specific m_F in the $5^2S_{1/2}$ state to a specific m_J in the $5^2P_{3/2}$ state will move as $\Delta E = (g_J m_J \mu_B - g_F m_F \mu_B)B$. If the distance between that peak and its symmetric neighbor (the transition from $-m_F$ to $-m_J$) is tracked, it should grow with twice that rate:

$$\frac{\mathrm{d}}{\mathrm{d}B}[\text{splitting}] = 2(g_J m_J \mu_B - g_F m_F \mu_B) \qquad (1)$$

This will be important later as a means of determining the g_J values for both $5^2S_{1/2}$ and $5^2P_{3/2}$.

II. APPARATUS

This experiment makes use of both (1) the MIT Junior Lab Doppler-free spectroscopy arrangment and (2) a pair of solenoidal electromagnets also donated by the MIT Junior Lab.

II.1. Doppler-free Equipment

The pre-existing optical board for Doppler-free spectroscopy is depicted in Figure 2. The TUI Optics laser, composed of a temperature-controlled 780nm AlGaAs semiconductor laser diode and coupled to a tunable external cavity, can output a single mode with linewidth below 30MHz.

A Faraday isolator protects the laser from any undesired feedback, after which part of the beam is split to a Fabry-Pérot cavity of length $54.9 \pm .4$cm.[4] The remaining beam is directed to a prism, wherein two small probe

[1] The first term can actually include further coupling structure [5] which does not affect this discussion.
[2] There is also a nuclear term in the expansion of g_F, but since $g_I \ll g_J$ the nuclear term will be neglected for our purposes.
[3] Neglecting the nuclear term again.
[4] The .4mm uncertainty in the cavity length arises from the difficulty of precisely identifying the locations of the mirror surfaces inside the protective mounts. However, this uncertainty is much smaller than other systematics.

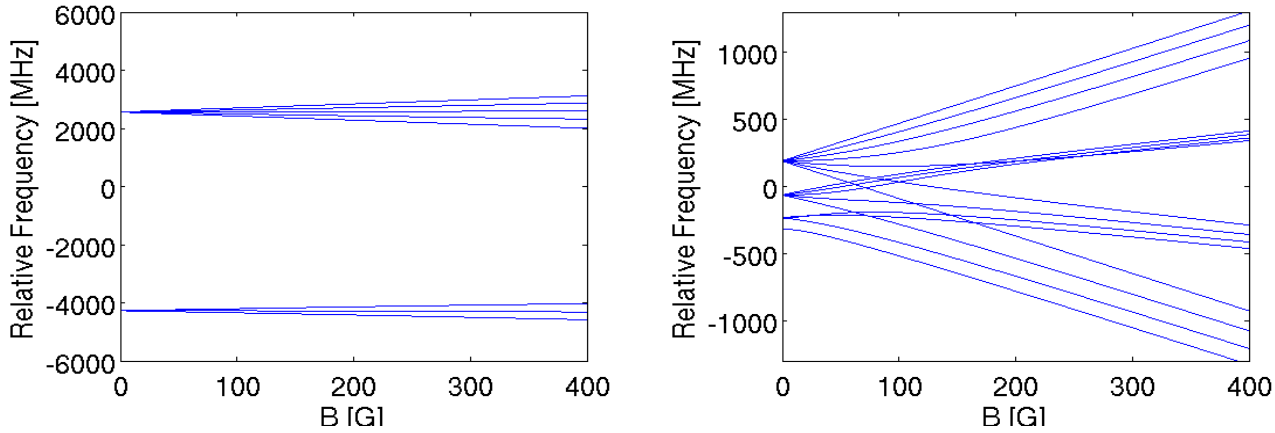

FIG. 1: Numerical diagonalization of the hyperfine-Zeeman Hamiltonian for $5^2S_{1/2}$ (left) and $5^2P_{3/2}$ (right) in ^{87}Rb. These plots show that the relevant B values of 160-300G keep $5^2S_{1/2}$ in the low-field regime (organized by F) and $5^2P_{3/2}$ in the high-field regime (organized by m_J). Results are qualitatively similar for ^{85}Rb, though there are more levels since ^{85}Rb has I=5/2 versus ^{87}Rb with I=3/2.

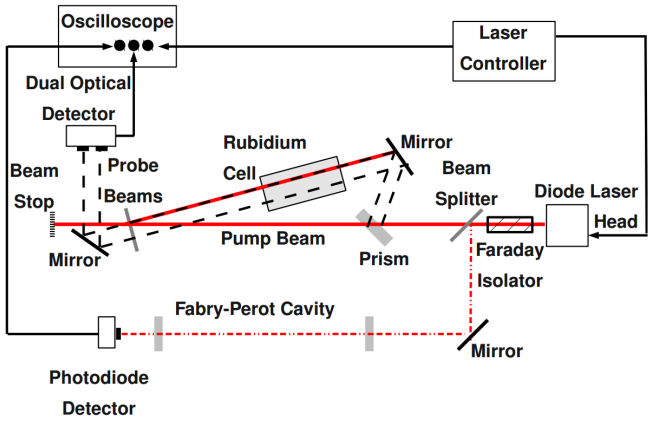

FIG. 2: The laser is split into a Fabry-Pérot signal (dash-dot red line), two probe beams (dashed black lines), and one pump beam (solid red line) which counter propagates along one of the probes.

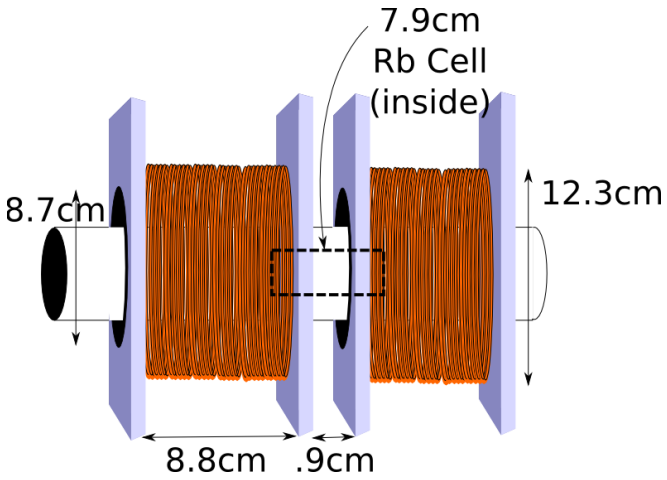

FIG. 3: Two solenoids with a small gap in-between supply the magnetic field to a Rubidium cell.

beams are split off, pass through the Rb cell (7.9±.1cm), and reach the dual detectors. The remaining laser light is reflected to counterpropagate through one of the probes. The difference of the detector voltages, as well as the Fabry-Pérot (FP) signal, is forwarded to the oscilloscope which is triggered by a sweep signal from the laser controller.

Additionally, neutral density filters (OD.1, OD.3) are placed in the pump beam path directly after the prism; this is found to improve the resolution of the Lamb peaks. Left or right circular polarizers, when employed, are placed directly after the beam splitter to allow only σ^- or σ^+ transitions respectively.

II.2. Electromagnets

Magnetic fields are supplied parallel to the axis of the Rb cell by two solenoidal electromagnets, as depicted in Figure 3. Each solenoid is 8.8cm long with 3400 turns of coil, and the inner diameter of each is 8.7cm, outer diameter 12.3cm. The two are placed along the same axis with a .9cm gap in between (that gap length does *not* include the .7cm plastic edges at the end of each coil). The solenoids are wired (not shown) in series to ensure equal currents, and the Rb cell is supported in the middle of the electromagnet by a PVC pipe.

To understand the magnetic field distribution that the sample will experience, this apparatus was modelled numerically as a combination of two "thick-coil solenoids" using the tools presented in [4]. Then, the electromagnet

was examined/calibrated empirically in two ways.

First, a perpendicular-field Hall probe was inserted through the .9cm gap to measure the magnetic field as a function of current for calibration, and the results are shown in Figure 4, wherein the model prediction of .3225G/mA is validated.

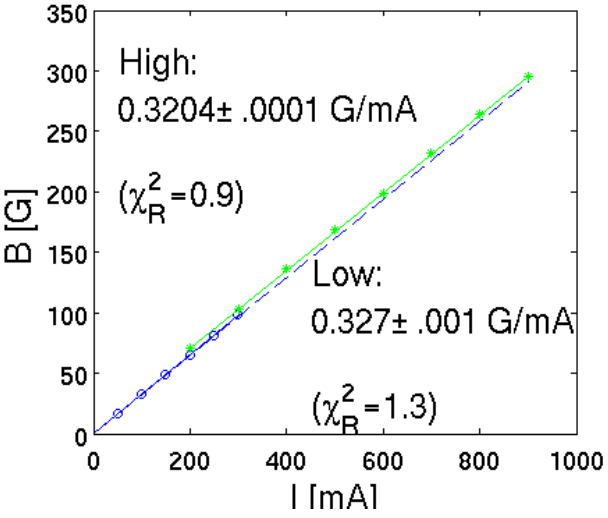

FIG. 4: Calibration of the solenoid magnetic field to current. The "low" data points (open circles) are measurements taken with the 300mA setting on the ammeter, while the "high" data points (filled) are measurements taken with the 10A setting. A linear fit (solid lines) is shown for each. The dotted line represents the theoretical prediction of 0.3225G/mA, and we see that this rate falls between the two observed slopes, confirming the validity of our model.

Second, an axial-field Hall probe was run along length of the tube to determine the spatial variation of the field (inhomogenous broadening). Although there was no reference suitable for calibrating the axial probe, this measurement, as shown in Figure 5, should still give an approximate validation of our model for the field variation. The plots show that, within a 7.9cm cell perfectly centered, we expect a 10% axial variation of B-field based on our model.

Because of the long dimensions of the perpendicular-field probe, it is not easy to verify the radial variation of the field; however, our model predicts that this is also on the order of 12.5% within the 2.5±.1cm diameter of the Rb cell (note that the center of the electromagnet, in the middle of the gap, is actually a local *minimum* of field strength). For error analysis, our magnetic field uncertainty will be taken as 12.5%.

III. QUALITATIVE RESULTS

At zero-field, we see the hyperfine Rubidium spectrum as reported previously [2]. This base-reference spectrum

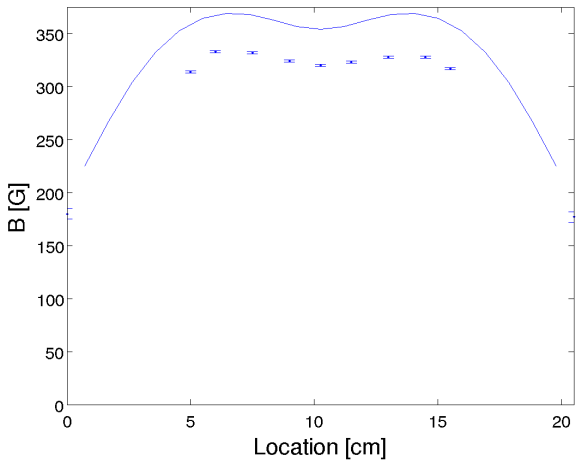

FIG. 5: Variation of the magnetic field along the axis of the probe. Since the axial probe calibration was unavailable, we don't expect to see the measurements (points with error bars) fall on the model (solid line). However, the general shape, if not scaling, of the measurements do match our predictions. Within a the length of the Rb cell, we see a ∼10% variation of field strength.

is shown in Figure 6. Overall linear sloping in this (and in all further spectra) has been substracted out. Note: the conversion from a time axis on the oscilloscope to a frequency axis on these plots (via peak-finding, and peak-fitting on the Fabry-Pérot, then fitting the identified frequency intervals to a quadratic) was discussed in great depth already [2]. The same strategy was implemented here, and, as the frequency uncertainty of a few megahertz is much smaller than the major contributors to error in this experiment, we will not repeat the extended discussion.

As we turn up the current beyond ∼45mA (∼15G), we enter the intermediate-field region of the $5^2P_{3/2}$ state, where both hyperfine and Zeeman effects are at play, and it rapidly becomes difficult to interpret the spectra due to the multitude of peaks splitting, crossing, and otherwise obstructing one another to the precision of our equipment. As we enter the high-field region (∼160G) and peaks organize by their m_j values, the signal becomes clearer. Furthermore, the legibility of the signal may be improved by the addition of a left- or right-circular polarizer to restrict the transitions as shown in Figure 7.

As shown, the left-circular polarizer (LCP) tends to highlight transitions to the left (higher frequency), and the opposite applies for the right-circular polarizer (RCP). So the LCP must favor transitions with a larger difference in energy, that is, those transitions upward which align the electronic magnetic moment to the field. Therefore, the LCP-allowed transitions will anti-align the electronic angular momentum from the field, corresponding to an addition of negative angular momentum along

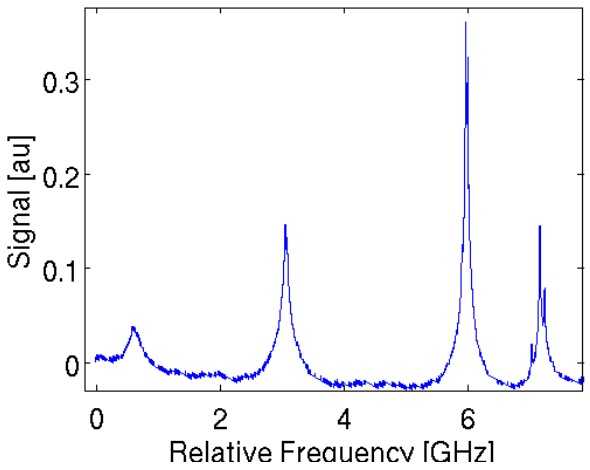

FIG. 6: Rubidium peaks at zero field, with no polarizers, clearly showing the hyperfine structure. Note: frequency increases *right-to-left*, as per convention with this experiment [5].

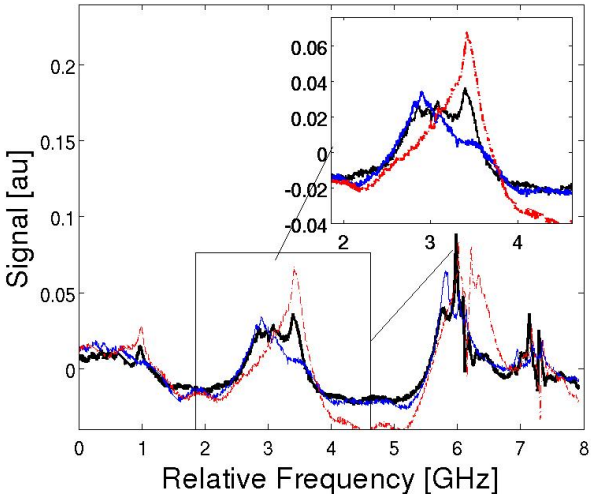

FIG. 7: The above spectra, taken at 400mA (130G), zooms in upon the second peak (transitions from ^{85}Rb $5^2S_{1/2}$ F=2). Polarizers help to clarify which peaks correspond to which transitions. Thick black line: no polarizers. Thin, solid, blue line: left-circular polarizer. Thin, dashed, red line: right-circular polarizer.

the quantization axis. By this chain of reasoning, LCP gives the σ^- transitions, and RCP the σ^+ transitions, which is consistent with a B-field pointing parallel to the probe beams (ie left in the coordinates of Figure 2).

Since spectra with different polarizations must be collected on different runs, the oscilloscope time (and thus relative frequency) axes are not precisely aligned. Therefore, it is not easy take peak differences between differently polarized spectra. All numerical analysis is done on the unpolarized spectrum which includes all the peaks, and the purpose of the polarized spectra is (1) to show that the data is actually demonstrating Zeeman splitting the way we expect and (2) to guide the experimenter's eyes in choosing which peaks to follow for analysis (as discussed below).

Given that the low- and intermediate- field data are so difficult to interpret, numerical work will focus upon the high-field data. The idea will be to examine the rate at which the σ^- transitions (as highlighted by LCP spectra) and σ^+ transitions (as highlighted by RCP spectra) diverge.

IV. QUANTITATIVE RESULTS

In order to determine the gyromagnetic ratios, we track the rate at which peaks separate within each $5^2S_{1/2}$ hyperfine group (see Figure 8).

Each group splits into two obvious Zeeman groups. Ideally, as in Figure 1, there should be a high-field Zeeman group for each allowed combination of the m_J values in the $5^2P_{3/2}$ state with each of the m_F values in the $5^2S_{1/2}$ state. However, there may be various approximate selection rules, which, combined with the linewidths in this data, obscure most of those peaks. Thus, we will have to match the observed peak motion to theoretically predicted motion in order to determine which peak groups we see. We will assume that, by the symmetry of the atomic physics which determines which transitions are visible, the two clear Zeeman groupings from each pair have quantum numbers which are precisely the negatives of one another (the condition for Equation 1).

There is generally one prominent peak from each Zeeman group which can be tracked well across the high-field range. So, to track each Zeeman group, that prominent feature is first located by hand at each value of the current, and then fitted by a Lorenztian, as in Figure 8. The distances between each peak pair are then regressed as a function of magnetic field, as shown in Figure 9.

The χ^2_R values for all the fits are .06 or below, which indicates that the magnetic field variation uncertainty used to generate the horizontal errorbars does not affect the fitting as strongly as imagined. Perhaps this fortunate result is because the magnetic field error is essentially the same for every data point. Nonetheless, this error component will be propagated through the remainder of the analysis, because it will constitute an overall uncertainty in the fitted rates themselves.

The slopes from these fits are shown in Table I, where statistical uncertainties come from the regression, and systematic uncertainties are dominated by the magnetic field variation as discussed in the calibration.

We then, using previously accepted values of the gyromagnetic ratios, calculate the splittings predicted from Equation 1, for the multiple allowable values of m_F and m_J. Typically, there is only one set of quantum numbers which could possibly match each rate in Table I (ie, only

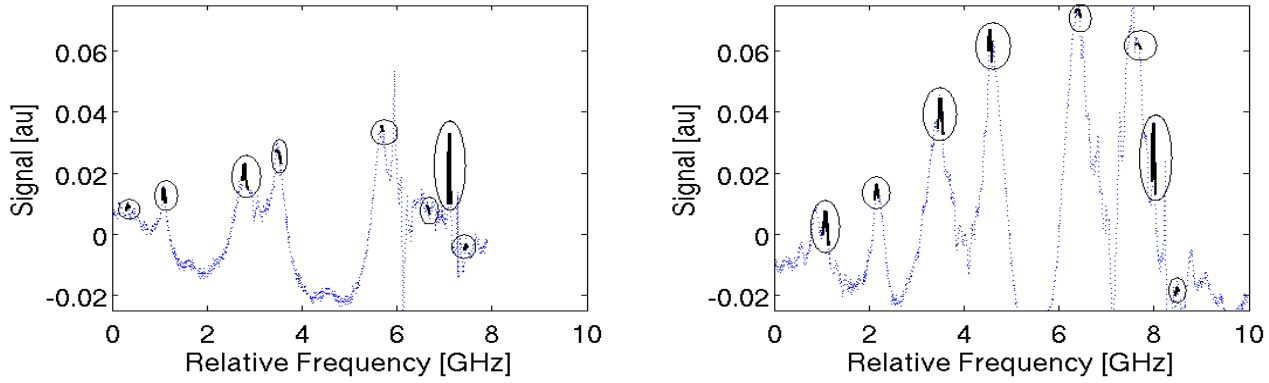

FIG. 8: The above eight peaks (two from each $5^2S_{1/2}$ hyperfine grouping) were identified by hand at 500mA (left), 600mA, 700mA, and 800mA (right), and then located precisely with Lorentzian fits. The increasing separation between the pair in each grouping was used to calculate the gyromagnetic ratios.

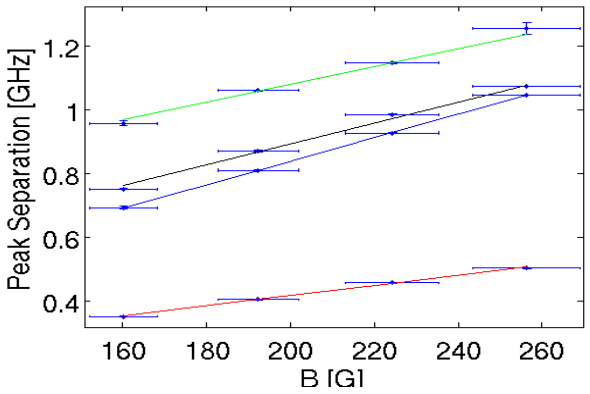

FIG. 9: Peak separation vs magnetic field for each group. Reading top to bottom, this correspond to transition groups from: (1) ^{85}Rb $5^2S_{1/2}$ F=3, (2) ^{87}Rb $5^2S_{1/2}$ F=1, (3) ^{85}Rb $5^2S_{1/2}$ F=2, (4) ^{87}Rb $5^2S_{1/2}$ F=2.

Isotope	F_{init}	Rate	σ_{stat}	σ_{sys}	Predicted
^{87}Rb	1	3.25	.23	.40	3.27
^{85}Rb	2	3.66	.01	.46	3.74
^{85}Rb	3	2.78	.14	.35	2.80
^{87}Rb	2	1.59	.05	.20	1.89

TABLE I: Rates at which the fitted peak pairs (labelled by isotope and F value in the $5^2S_{1/2}$ state) separate, and comparison with predicted values. [MHz/G].

one m_F, m_J combination produces a rate near the given error bars for each group). Since our uncertainties thus give us enough precision to identify which set of quantum numbers to work with for each group, we then use those quantum numbers in converting our rates into the gyromagnetic ratios. For reference, the quantum numbers are shown in Table II, and the corresponding theoretical rates are included in Table I.

Given the rates at which these peaks split, and their

Isotope	F_{init}	m_F	m_J
^{87}Rb	1	1	1/2
^{85}Rb	2	2	1/2
^{85}Rb	3	-1	1/2
^{87}Rb	2	0	1/2

TABLE II: The identified quantum numbers of the peak pairs.

quantum numbers, we use Equation 1 to generate a linear system for the rates in terms of the g-factors. Since the g-factors for ^{87}Rb and ^{85}Rb are identical (to within 10ppb), this is a system of four equations in two variables.

Inverting the system and propagating the uncertainties through the linear equations, we arrive at the results in Table III, which are consistent with previously accepted values [1].

State	g_j	σ_{stat}	σ_{sys}	Accepted
$5^2S_{1/2}$	2.24	.11	.48	2.00
$5^2P_{3/2}$	1.18	.05	.16	1.34

TABLE III: The g_J values determined from the splitting rates, and their previously accepted values.

V. CONCLUSION

By focusing on the region of magnetic fields which gave a low-field approximation for $5^2S_{1/2}$ and a high-field approximation to $5^2P_{3/2}$, we were able to generate clear enough spectra to analyze the Zeeman effect in rubidium. Tracking the movement of peak groups through these spectra then enabled us to measure the gyromagnetic ratios for the electronic angular momentum of both states, and values found are consistent with previous observations.

[1] E. Arimondo, M. Inguscio, and P. Violino. Experimental determinations of the hyperfine structure in the alkali atoms. *Rev. Mod. Phys.*, 49:31–75, Jan 1977.
[2] Sam Bader and Leo Zhou. Doppler-Free Spectroscopy of the Hyperfine Structure in Rubidium. *MIT Junior Lab*, 2013.
[3] Sam Bader and Leo Zhou. Observing the Zeeman Effect with Doppler-Free Spectroscopy. *MIT Junior Lab*, 2013.
[4] Thomas J Corona. Tools for Electromagnetic Field Simulation in the KATRIN Experiment. Master's thesis, MIT, 2009.
[5] MIT Department of Physics. Doppler-free spectroscopy.
[6] Daniel A. Steck. Quantum and atom optics.